Reconstruction of Ultra-thin Alveolar-capillary Basement Membrane Mimics

Puja Jain, Akihiro Nishiguchi, Georg Linz, Matthias Wessling, Andreas Ludwig, Rolf Rossaint, Martin Möller, and Smriti Singh*

Alveolar-capillary basement membrane (BM) is ultra-thin (<2 µm) extracellular matrix that maintains integral epithelial-endothelial cell layers. In vitro reconstructions of alveolar-capillary barrier supported on synthetic scaffolds closely resembling the fibrous and ultra-thin natural BM are essential in mimicking the lung pathophysiology. Although BM topology and dimensions are well known to significantly influence cellular behavior, conventionally used BM mimics fail to recreate this natural niche. To overcome this, electrospun ultra-thin 2 µm poly(caprolactone) (PCL) nanofibrous mesh is used to establish an alveolar-capillary barrier model of lung endothelial/epithelial cells. Transepithelial electrical resistance (TEER) and permeability studies reveal integral tight junctions and improved mass transport through the highly porous PCL meshes compared to conventional dense membranes with etched pores. The chemotaxis of neutrophils is shown across the barrier in presence of inflammatory response that is naturally impeded in confined regions. Conventional requirement of 3 µm or larger pore size can lead to barrier disruption due to epithelial/endothelial cell invasion. Despite high porosity, the interconnected BM mimic prevents barrier disruption and allows neutrophil transmigration, thereby demonstrating the physiological relevance of the thin nanofibrous meshes. It is envisioned that these bipolar cultured barriers would contribute to an organ-level in vitro model for pathological disease, environmental pollutants, and nanotoxicology.

1. Introduction

Respiratory diseases affecting the lung parenchyma like pneumonia, tuberculosis, pulmonary edema, lung cancer, acute respiratory distress syndrome (ARDS), and the recent pandemic of SARS-CoV-2 which is known to access host cells via angiotensin-converting enzyme 2 (ACE2) present on the alveolar type II cells[1] are one of the major cause of morbidity in the world. The global presence of these diseases and their effect on human health and economy highlights the importance to better understand the lung pathophysiology for the development of new therapies. A greater part of our understanding of lung pathophysiology in healthy and disease states stems from experimental animal models,[2] but the cost and ethical issues have restricted their use. Moreover, the translation of results obtained across different species into human clinical trials is still challenging.[3] To overcome these challenges, 3D in vitro models that can recreate artificial cellular microenvironments of the lung parenchyma are sort for. To mimic the alveolar function, in vitro alveolar-capillary barrier models are constructed. These models

P. Jain, Dr. A. Nishiguchi, G. Linz, Prof. M. Wessling, Prof. M. Möller, Dr. S. Singh
DWI-Leibniz Institute for Interactive Materials
Forckenbeckstr. 50, 52056 Aachen, Germany
E-mail: singh@dwi.rwth-aachen.de
Dr. A. Nishiguchi
Center for Functional Materials
National Institute for Materials Science
1-1 Namiki, Tsukuba, Ibaraki 305-0044, Japan

The ORCID identification number(s) for the author(s) of this article can be found under https://doi.org/10.1002/adbi.202000427.

G. Linz, Prof. M. Wessling
Chemical Process Engineering
RWTH Aachen University
Forckenbeckstr. 51, 52056 Aachen, Germany
Prof. A. Ludwig
Institute for Molecular Pharmacology
University Hospital RWTH Aachen University
Wendlingweg 2, 52074 Aachen, Germany
Prof. R. Rossaint
Department of Anesthesiology
University Hospital RWTH Aachen University
Pauwelsstr. 30, 52074 Aachen, Germany
Dr. S. Singh
Max Planck Institute for Medical Research (MPImF)
Jahnstrasse 29, 69120 Heidelberg, Germany

**ADVANCED
SCIENCE NEWS**
www.advancedsciencenews.com

**ADVANCED
BIOLOGY**
www.advanced-bio.com

commonly consist of a bipolar culture of confluent endothelial and epithelial cell layers, which are separated by a polymeric membrane to support and separate the different cell layers.[4]

However, despite the recent progress, the in vitro reconstruction of the alveolar barrier lacks important aspects of the structural elements present in vivo.[5] We are convinced that one of the drawbacks of most in vitro models refers to the communication between the endothelial and the epithelial cell layers,[6] which originates from the use of polymeric membrane as a basement membrane (BM) mimic. The natural BM is 0.1 to 2 µm thick and is mainly composed of collagen IV, laminin, and proteoglycans.[7] The very thin BM with characteristic fibrous topology imparts structural integrity with the concomitant presence of interconnected pores that range between 10–150 nm and are responsible for the selective transport of solutes and proteins across it.[8] However, in most alveolar-capillary barrier models, synthetic microporous membranes are fabricated from polycarbonate (PC), poly(dimethylsiloxane) (PDMS), or poly(ethylene terephthalate) (PET) with track-etched pores.[9] These membranes are either available as transwell systems or molded as in the case of PDMS and are chosen because of their easy handling as they provide a good substrate for the seeding of confluent cell layers. Nevertheless, these membranes are relatively thick with thickness ranging to 10 µm or more. Despite a pore size range of 0.4 to 8 µm, their porosity is small due to limitations in track etching techniques compared to the natural BM.[10] Thickness, porosity, and pore sizes of membranes used in co-culture systems are essential features as they are involved in maintaining physical contact between cells on opposite sides, paracrine signaling, as well as the transmigration of immune cells across the alveolar barrier.[4b,11]

The relevance of pore size has further been reported in the construction of the alveolar barrier, where the endothelial cells invaded the opposite side of the membrane in presence of large pores (3–10 µm), thereby disrupting the separated cellular layers that constitute a barrier system.[12] This can impede the cellular crosstalk between the endothelial and epithelial in health and disease states by clogging of the pores.[6] Additionally, disruption of endothelial cell layers by invading epithelial cells across membranes with pores 3 µm or large has also been observed.[13]

To study inflammatory response during lung injury, it is imperative to investigate the neutrophil chemotaxis across the alveolar-capillary barrier, as neutrophils are an important part of the innate immune system.[14] The influx of neutrophil into the extravascular compartments of the lungs delineates pathological conditions like ARDS,[15] chronic obstructive pulmonary disease (COPD),[14d] etc. Following infection, neutrophils migrate across the endothelium, through the BM, and across the epithelium into the airway.[16] In ARDS this migration can further lead to epithelial, endothelial cell death, barrier permeability which in turn can cause alveolar edema.[14c] The mechanism by which neutrophils migrate across the alveolar barrier is still unclear.[17] One of the main reasons for this is the unavailability of an appropriate model. Since neutrophil migration is impeded in confined regions that are nearly 10% of its nucleus size (2 µm²) with cross-sectional areas of 1–2 µm² that correspond to nearly 1 µm pore diameters,[18] in vitro models which are used for neutrophil transmigration assays require the presence of 3 µm or larger pore size membranes.[19] But, the characteristic behavior

of epithelial and endothelial cell invasion in presence of large pores can disrupt the barrier integrity and can lead to false readouts.[12,13] This is contrary to the natural alveolar barrier, where the cell layers are separated by the BM irrespective of its reduced thickness, while the interconnected pores regulate signal transfer across cell layers by allowing passive diffusion of small molecules[20] while normal cells can traffic across freely and rapidly during morphogenesis and immune surveillance by activation of tissue-invasive programs.[21]

Therefore, an efficient and physiologically relevant in vitro alveolar–capillary barrier requires characteristically ultra-thin BM mimic with structural complexity to mimic the functional aspect of the lung. We previously reported the fabrication of electrospun BM mimic which was bio-functionalized with covalently bound RGD and laminin peptides for the development of a bipolar alveolar-capillary co-culture model.[10d] Moreover, the use of electrospinning to fabricate membranes is a better technique to replicate the fibrous structure of the ECM as well as the ability to control properties including mesh alignment, thickness, fiber diameter, mechanical properties to better mimic BM.[22]

However, in reference to our previous work, the question about reducing the thickness of the BM to its naturally occurring form (≤2 µm) remained unresolved due to challenges in the fabrication and stability of the alveolar-capillary barrier for a longer duration of time. In the present work, 2 µm nanofibrous PCL mesh represents a BM mimic that is structurally analogous to its natural form and supports both the endothelial and epithelial cell layers on opposite sides to constitute an alveolar–capillary barrier for 21 days. The significance of altering BM mimic structure and thickness is exemplified by comparing properties of the alveolar barrier on 2 µm PCL mesh with the commonly used commercial transwell insert comprising of a 10 µm thick PET membrane as control. The alveolar-capillary barrier was investigated for barrier integrity; ECM production and migration of neutrophils in response to an inflammatory stimulus.

2. Results and Discussion

2.1. Nanofibrous Mesh Characterization

Non-woven electrospun PCL nanofiber mesh was fabricated to mimic barrier architecture and function, and 10 µm thick PET membranes with 0.4 µm pore size were used as control. Keeping all other parameters of electrospinning constant (Table S2, Supporting Information) time and flow rate of spinning was optimized to attain meshes of different thicknesses. The thickness of the ultrathin mesh was accurately measured by the white light interferometer. To ascertain this, the meshes were mounted on a silicon wafer and white light was passed through it. The in-built software of the interferometer was used to determine the size of the step created by the mesh on the silicon wafer (**Figure 1**A) while the thickness of the meshes was determined by measuring the difference in height between the upper and lower surface. The spinning time of 1 min, 21 kV, 15 cm (distance between collector and spinneret) resulted in meshes with 2 µm thickness which were selected for further analysis and development of the alveolar-capillary barrier. The meshes were further analyzed using field emission scanning
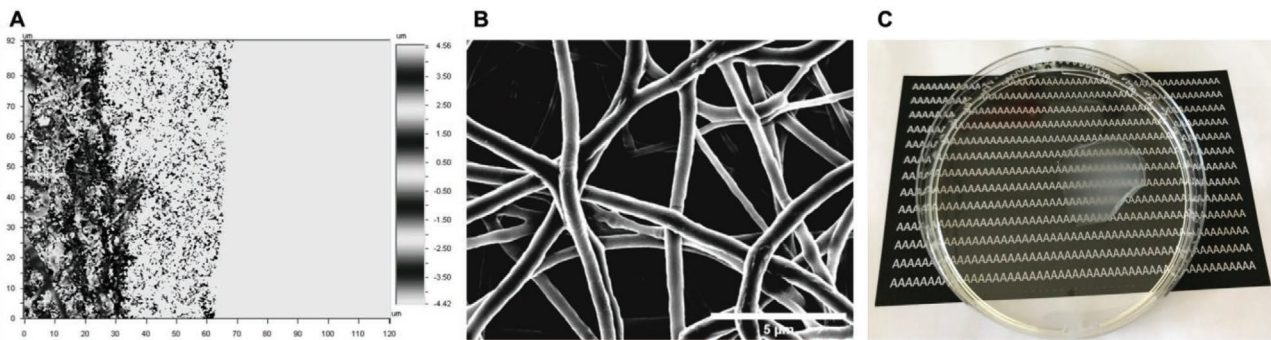
Figure 1. Characterization of the PCL nanofiber meshes where A) white light profilometer is used to determine mesh thickness by step analysis using in-built software with an average thickness of 2 µm; B) Scanning Electron Micrograph image is analyzed by ImageJ software to quantify fiber diameter and pore area; C) ultra-thin optically transparent nanofibrous PCL mesh.

electron microscopy (FESEM) images and displayed well-defined and monodispersed fibers (Figure 1B). The images were probed using the plugin diameterJ provided by ImageJ software to determine the mean fiber diameter and pore area. The analysis revealed fibers with an average diameter in the range between 260–350 nm and the mean pore area was calculated to be 1.66 µm². The equivalent pore diameter was calculated using the following equation:

$$Sqrt(4A)/pi \tag{1}$$

where A represents the mean pore area and an equivalent pore diameter of 1.45 µm was determined. Compared to the natural BM (10–150 nm) the calculated equivalent pore diameter of the nanomesh is higher and not an absolute representation of the actual pore size. This is due to the 2D observation of the mesh where the pore size is calculated using the electron microscopy image.[23] The nonwoven mesh is fabricated by layer by layer deposition of the fibers, this results in the formation of interconnected pores where the actual pore size is lower than the calculated equivalent pore diameter from the 2D section. The Young's modulus of PCL nanofiber meshes was measured to be 9.7 MPa (Figure S3, Supporting Information), which is significantly close to the elastic modulus of alveolar BM which ranges between 2 to 3 MPa.[24] whereas the elastic modulus of the control PET membranes ranges from 2–3 GPa which is three orders of magnitude higher than the native BM.[25] Material elasticity has a great impact on cell behavior including ECM deposition, morphology, and display of focal adhesion.[26] Stiff substrates resemble physiology similar to that of a fibrotic tissue, where cellular behavior can result in a pathological function.[27] Thus the PCL nanofiber mesh is a closer representation of the physiological BM in terms of elastic modulus as well as architecture when compared to the widely used PET membranes.

2.2. Barrier Integrity of In Vitro Alveolar–Capillary Models
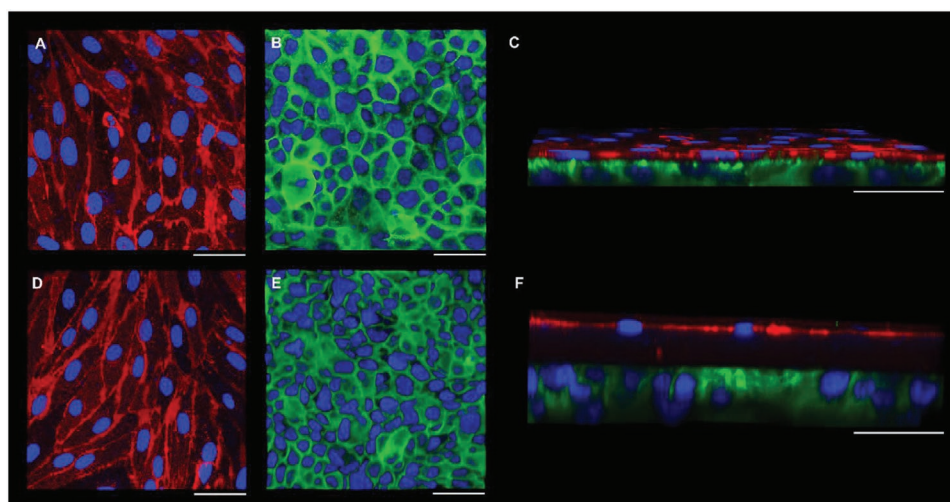
2.2.1. Alveolar–Capillary Barrier Formation

To establish the alveolar-capillary barrier, human pulmonary microvascular endothelial cells (HPMEC) and human distal lung epithelial cell line NCl-H441 were used.[4a] NCI-H441 cell lines are characterized by similarities of surfactant production to alveolar type II cells and are often used due to their high barrier integrity to replace primary alveolar epithelial cells which are difficult to maintain during long term culture conditions.[28] On reaching confluence and differentiation, the model was examined for the establishment of cell-cell junctions and the formation of a tight epithelial barrier. Reducing the thickness of the BM mimic for the establishment of a long term alveolar-capillary barrier imposes challenges towards the integrity and stability of cell layers. To investigate this immunofluorescence staining of cell junction protein CD31 in HPMEC and junctional complexes E-cadherin in H441 cell layers was performed and analyzed using confocal laser scanning microscopy (CLSM). The CLSM and light micrograph images show well-organized CD31 and E-cadherin and intact barrier function (**Figure 2**A–C and Figure S5, Supporting Information) respectively on the 2 µm PCL meshes and PET membranes (Figure 2D–F). Despite the reduced thickness of BM mimic, no cell infiltration from either of the layers was observed (Figure 2C). This could be attributed to the architecture of the nanofibrous mesh where the interconnected pores allow for the cell-cell communication but prevent cell infiltration as in the natural BM. Similarly, distinct cell layers were observed on the control PET membrane separated by a thickness of 10 µm (Figure 2F).
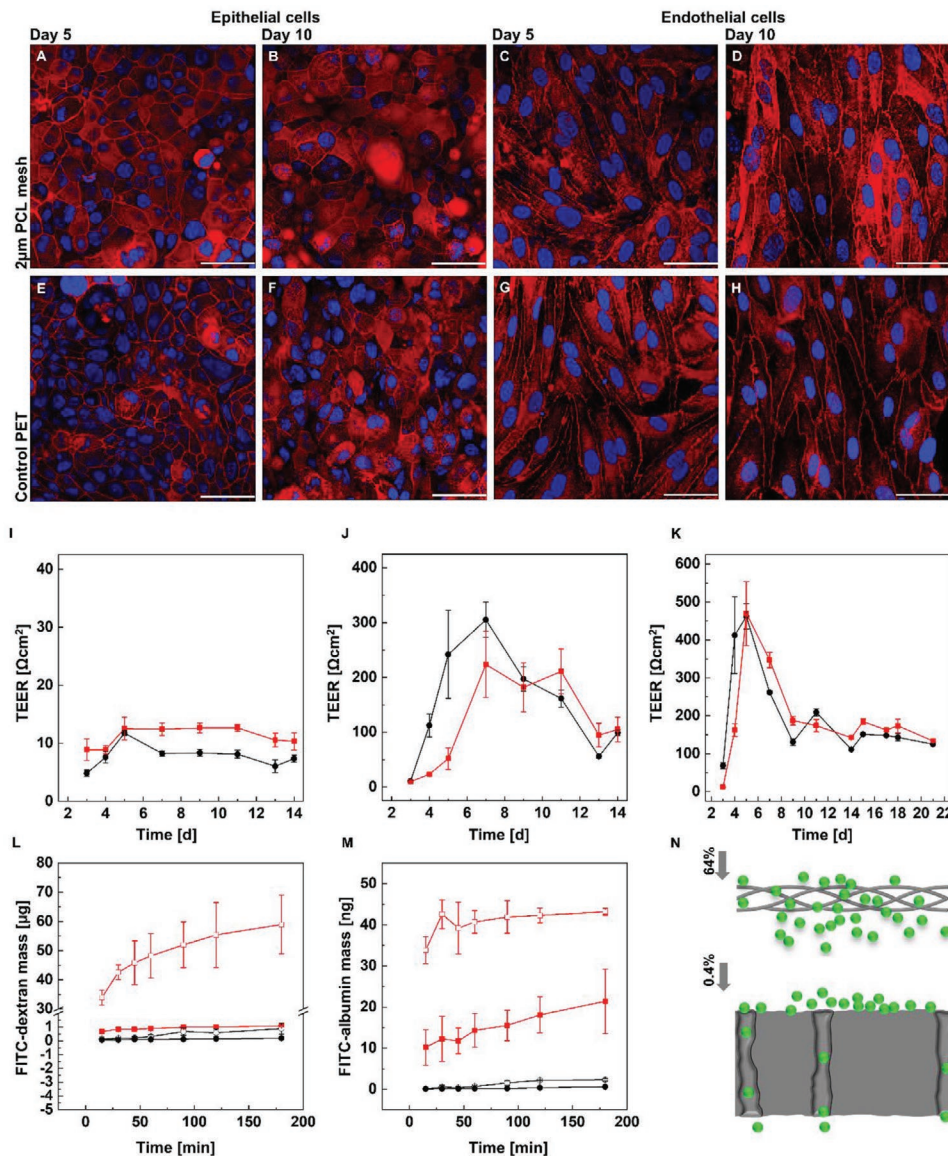
2.2.2. Tight Junctions and Barrier Properties

Further assessment of barrier integrity was carried out by immune-staining cellular tight junctions (ZO-1) and Transepithelial electrical resistance (TEER) measurements which represent the restriction to the movement of ions across the paracellular path between adjacent cells. Tight junctions between epithelial cells in the alveolar barrier prevent the cytokines, toxins, and pathogens from infiltrating the epithelial layer and regulates the permeability of solutes and ions through the paracellular space. Other junctions, particularly adherens junctions further contribute to barrier function by regulating tight junction assembly.[8b,29] Intact formation of tight junctions (ZO-1) on epithelial and endothelial cells was observed (**Figure 3**) on alveolar models on PCL and PET membranes. The presence of intact tight and adherens junctions in

2000427 (3 of 13)

Figure 2. CLSM images showing the immuno-stained endothelial cell-specific marker (CD31-red), epithelial adherens junction (E-cadherin-green), and cell nucleus (DAPI-blue) in the alveolar–capillary barrier established on 2 μm PCL nanofibrous meshes and control (PET membranes); A,D) cell contact junctions of HPMEC on PCL and control membranes respectively; B,E) adherens junction of H441 cells on PCL and control membranes respectively; C,F) correspond to the cross-sectional view of the barrier on PCL and control membranes. The immuno-stained images display no cell layer infiltration in the ultra-thin and porous PCL meshes. Scale bar: 50 μm.

the model shows the formation of a functional in vitro alveolar-capillary barrier. Moreover, a high TEER value indicates strong tight junctions between polarized cells across a monolayer. Real-time TEER measurements were carried out from day 3 to day 21 on the alveolar-capillary barrier and monocultures of H441 and HPMEC established on PCL meshes. As a control, co-culture and monocultures on PET membrane were used. It was observed that the TEER values increased after the addition of dexamethasone (1 μM) on day 4 which is similar to the earlier works of Hermanns et al., where the addition of glucocorticoid dexamethasone is shown to enhance the barrier properties of the epithelial cells and thereby increases the TEER.[30] A similar trend was observed on both the PCL meshes and the control. The resistance on monolayer H441(Figure 3J) and alveolar-capillary barrier (Figure 3K) peaked between day 4 and day 7 followed by a stable drop on day 9 and maintained a plateau phase thereon. As expected, the alveolar-capillary barrier had higher resistance (stronger tight junctions) compared to the monoculture of H441 and HPMEC (Figure 3K). The TEER values of monoculture HPMEC (Figure 3I) were far lower than that of H441 cell monolayers (Figure 3J) as it is the epithelial cells that form the tight junction and are responsible for the barrier integrity.[30] Peak TEER values of alveolar-capillary barrier reached 462 Ωcm^2 on control and 470 Ωcm^2 on PCL meshes (Figure 3K), where PCL meshes display a plateau phase slightly higher than that of control. This indicates the stable development of a uniform epithelial cell layer with integral cellular tight junctions essential for the development of an intact alveolar-capillary barrier on the ultra-thin 2 μm PCL meshes. The drop in the TEER values after day 7 is most likely due to the used cell seeding density of the NCI-H441 epithelial cells. Since the PCL membranes are very thin an initial cell density of 1×10^5 cells cm^{-2} is used which may lead to the formation of multilayered cells which contributes to the initial high TEER values. However, a single monolayer of epithelial cells is an important characteristic of the alveolar barrier and this is achieved by the addition of dexamethasone after 3 days of co-culture and has previously been reported by Hermanns et al.[4a] Formation of stable epithelial monolayers on the addition of dexamethasone from the multi-layered epithelial layer can lead to a decrease in the TEER values. In addition to TEER, the integrity of intercellular junctions was evaluated by macromolecular permeation of FITC-dextran (70 kDa) and FITC-albumin (66 kDa). Permeation of FITC-dextran with time reveals the paracellular movement of the tracer molecule from the epithelial to the endothelial compartment, while permeation of FITC-albumin can occur either through paracellular or transcellular routes across cell layers.[31] Permeation properties of day 10 alveolar-capillary barriers were compared when the TEER values were stabilized. The permeation assay of FITC-dextran and FITC-albumin reveals that a significantly low amount of molecules move across the cell layers on both the PCL mesh as well as the PET membrane in comparison to the amount across the blank membranes ((Figure 3L,M) and **Table 1**). However, the passage of FITC-dextran across the blank PCL meshes is significantly higher than that across the blank PET membrane. This is indicated by the mass flux of FITC-dextran, which is the number of molecules that pass across the membrane in 60 min on both the blank membranes. The calculated mass flux of 64% on the blank PCL meshes compared to a mere 0.4% mass flux across the blank PET membranes indicate the highly permeable nature of the PCL meshes (Figure 3N). This could be attributed to the difference in the structure of the two membranes; the etched 0.4 μm pores of the control membranes are less dense in number compared to the larger interconnected pores present in the PCL meshes. Highly porous PCL meshes allow higher permeation compared to the control, which is important for physiological cell-cell communication. Transmission electron microscopy (TEM) was used to further investigate the alveolar–capillary barrier on the membranes. TEM images of the

**ADVANCED
SCIENCE NEWS**

www.advancedsciencenews.com

**ADVANCED
BIOLOGY**

www.advanced-bio.com

Figure 3. CLSM images showing the immuno-stained tight junctions (ZO-1 red) of both the endothelial and epithelial cell layers and cell nucleus (DAPI-blue) in the alveolar–capillary barrier established on 2 µm PCL nanofibrous meshes and control (PET membranes); A,E) day 5 tight junctions of H441 cell layer side on PCL and control membranes respectively; B,F) day 10 tight junctions of H441 cell layer side on PCL and control membranes respectively; C,G) day 5 tight junctions of HPMEC cell layer side on PCL and control membranes respectively; D,H) day 10 tight junctions of HPMEC cell layer side on PCL and control membranes respectively. Scale bar: 50 µm. Permeability of tight junctions is assessed by TEER (Ωcm^2) on I) monolayer of HPMEC; J) H441; and K) alveolar–capillary barrier on PCL meshes (red) and control (black). TEER values are the highest in the alveolar–capillary barrier compared to the monolayer of H441 and HPMEC. The high TEER value indicates stronger tight junctions of the alveolar-capillary barrier on PCL meshes and is stable for 21 days of the culture period. $n = 3$; Amount of permeated L) FITC-dextran (70 kDa) and M) FITC-albumin (66 kDa) across alveolar–capillary barrier on PCL meshes (red filled square) and control (black filled circle) with time in minutes. $n = 3$; N) schematic of permeation of molecules across blank PCL mesh and PET membrane where highly permeable meshes allow 64% molecules to pass across compared to 0.4% across the PET membrane. $n = 3$.

control show pore blocking by endothelial/epithelial cellular extensions (Figure S6, Supporting Information) that impede the macromolecular permeation. Thus, the PCL nanofibrous meshes not only resemble in architecture and thickness of the BM but also allow efficient cell signaling and molecule permeation due to their highly porous structure, while maintaining a clear separation between the cells on opposite sides of the barrier.

2.3. Effect of TNF-α on Paracellular Integrity and Adhesion Molecule ICAM

Cytokines like Tumour Necrosis Factor-α (TNF-α) and Interleukin 8 (IL-8) are pro-inflammatory cytokines involved in inflammatory lung diseases.[32] These inflammatory cytokines induce the expression of intercellular adhesion molecule-1 (ICAM-1) in endothelial cells. ICAM-1 is a transmembrane

**ADVANCED
SCIENCE NEWS**

www.advancedsciencenews.com

**ADVANCED
BIOLOGY**

www.advanced-bio.com

Table 1. Apparent permeability values of FITC-dextran and FITC-albumin across an alveolar–capillary barrier. The values indicate the formation of integral barrier properties on both the PCL mesh as well as the PET membrane. $n = 3$; where values are indicated as mean ± standard error.

| Alveolar–capillary barrier on	Apparent permeability of FITC-dextran (cms^{-1})	Apparent permeability of FITC-albumin (cms^{-1})
2 µm PCL	$1.458 \times 10^{-6} \pm 3.794 \times 10^{-7}$	$1.982 \times 10^{-5} \pm 5.246 \times 10^{-6}$
10 µm control	$1.328 \times 10^{-6} \pm 2.530 \times 10^{-7}$	$2.404 \times 10^{-7} \pm 1.032 \times 10^{-7}$

glycoprotein that acts as ligands for leukocyte adhesion and transmigration to the site of inflammation in the lung.[33] Various cell types express ICAM-1 in low levels, however, in response to the pro-inflammatory cytokines its expression is upregulated. Similar to pulmonary inflammation, the response of TNF-α, IFNγ and their combination was investigated on the alveolar-capillary barrier model. The model was stimulated on the apical side with TNF-α (10 ng mL^{-1}), IFNγ (30 ng mL^{-1}) and their combination (TNF-α+IFNγ (10 ng mL^{-1} + 30 ng mL^{-1})) for 24 h. The apical and basal sides of the alveolar model were investigated separately for the quantification of released soluble ICAM-1 (sICAM). Surprisingly, low amounts of sICAM were found in the basolateral side compared to the apical side of the co-culture on stimulation with cytokines on the apical side (**Figure 4**). The concentration of sICAM values detected on the basolateral side of PCL meshes were, for untreated (28.742 ± 4.812 ng mL^{-1}), treated with TNF-α (39.310 ± 2.467 ng mL^{-1}), IFNγ (28.217 ± 6.837 ng mL^{-1}), and TNF-α+IFNγ (26.424 ± 3.320 ng mL^{-1}). Similarly, the concentrations of sICAM detected on the basolateral side of PET membranes were, for untreated (44.015 ± 14.942 ng mL^{-1}), treated with TNF-α (36.068 ± 0.704 ng mL^{-1}), IFNγ (30.784 ± 4.497 ng mL^{-1}), and TNF-α+IFNγ (34.316 ± 7.273 ng mL^{-1}). Thus, the values obtained for the basal side were low and not significantly different in all the stimulated and unstimulated conditions. This is similar to that observed by Jennifer et al., where co-culture models of H441 and ISO-HAS endothelial cells demonstrate an increase of sICAM on the apical side compared to the basolateral side when exposed to cytokines on the apical side.[34] The sICAM concentrations detected on apical side of PCL meshes

were, for untreated (83.087 ± 4.346 ng mL^{-1}), treated with TNF-α (75.223 ± 7.905 ng mL^{-1}), IFNγ (158.005 ± 3.021 ng mL^{-1}), and TNF-α+IFNγ (145.5877 ± 3.435 ng mL^{-1}). Similarly, concentrations of sICAM detected on apical side of PET membranes for untreated (63.013 ± 15.149 ng mL^{-1}), treated with TNF-α (61.523 ± 16.556 ng mL^{-1}), IFNγ (88.923 ± 13.493 ng mL^{-1}), and TNF-α+IFNγ (76.341 ± 14.569 ng mL^{-1}). Surprisingly, no difference in sICAM on unstimulated and TNF-α stimulated models was observed. This is due to the influence of dexamethasone that was added during the co-culture period and is frequently reported to inhibit the influence of TNF-α on cells.[34,35] However, there was a significant increase in sICAM on the apical side when stimulated with IFNγ and the combination (TNF-α+IFNγ) on both the PCL and PET membrane. The difference in sICAM production by the alveolar epithelial and endothelial cells despite their proximity, has also been observed and is reported due to the difference in the shedding mechanism of sICAM which is influenced by the complex mixture of proteases and anti-proteases in the microenvironment.[36]

Furthermore, the barrier integrity on exposure to the above cytokines was assessed by investigating the permeation of FITC-dextran across the barrier. As seen in Figure 4B, no significant difference in the permeation of FITC-dextran between TNF-α treated and untreated models was detected, which signifies an absence of barrier disruption. This is similar to the condition in lung parenchyma where TNF-α independently does not cause barrier dysfunction but the presence of additional factors such as LPS could lead to edema.[37] Surprisingly, no barrier disruption was observed on IFNγ stimulated models. However, it is worthy to point out that role of IFNγ on barrier
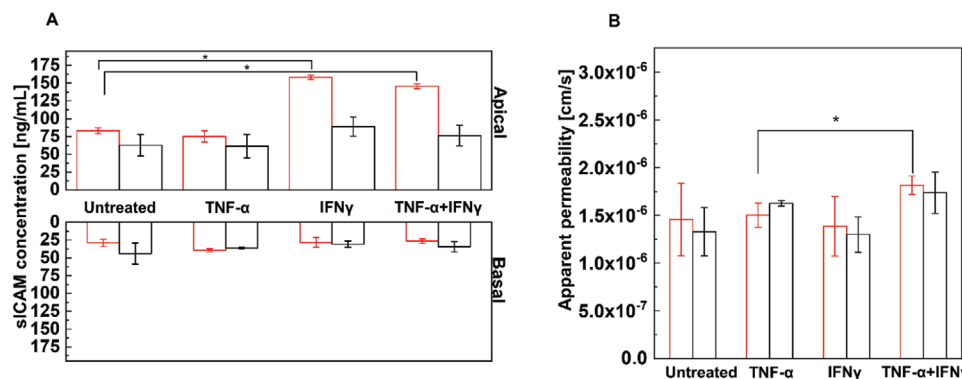
Figure 4. The immune response in terms of an increase in the amount of signaling proteins sICAM and degradation of intercellular tight junctions of the alveolar–capillary barrier on PCL nanofibrous meshes (red) and control (PET membrane-black) on apical exposure to the cytokine TNF-α (10 ng mL^{-1}), IFNγ (30 ng mL^{-1}) and TNFα+IFNγ (10 + 30 ng mL^{-1}) for 24 h are represented in graph. A) A significant increase in the apical concentration of sICAM in presence of IFNγ is observed compared to the untreated models and low basal sICAM concentration for all stimulated and unstimulated models $n = 2$; B) no significant difference in permeation of FITC-Dextran(70 kDa) across all TNF-α treated and untreated barrier models implies an absence of barrier disruption, however an increase in permeation is observed in presence of both TNF-α + IFNγ, Statistical analysis is carried out as mentioned in the experimental section where asterisks indicate alpha value $p < 0.05$ as "*". $n = 3$.

2000427 (6 of 13)
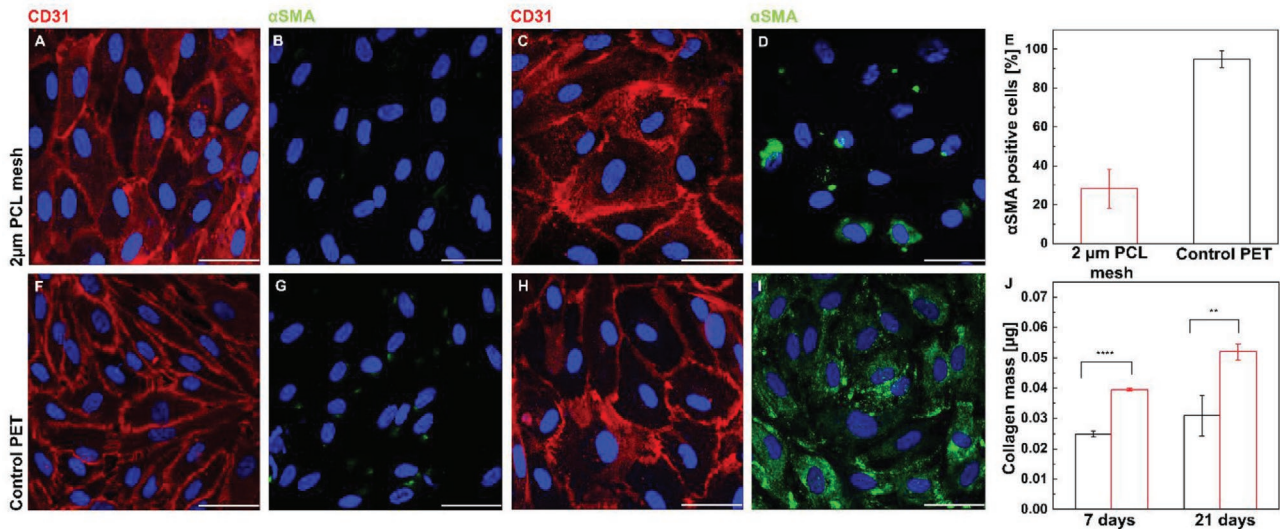
Figure 5. CLSM images showing the immuno-stained endothelial adherens junctions (CD31 red), mesenchymal marker αSMA (green), and cell nucleus (DAPI-blue) in the alveolar–capillary barrier established on 2 µm PCL nanofibrous meshes and control (PET membranes); A,B) day 7 models depict CD31 and αSMA on PCL meshes respectively; F,G) day 7 models depict CD31 and αSMA on PET membranes respectively; C,D) day 21 models depict CD31 and αSMA on PCL meshes respectively; H,I) day 21 models depict CD-31 and αSMA on PET membranes respectively; Scale bar: 50 µm. E) Percentage of endothelial cells expressing αSMA on 21 days barrier models on PCL mesh (red) and PET membrane (black); J) Indirect quantification of total collagen by hydroxyproline colorimetric assay on alveolar–capillary barrier models in culture for 7 and 21 days on PCL meshes (red) and control PET membranes (black). Significant collagen deposition observed on PCL meshes after both 7 and 21 days indicates cellular interaction with the fibers and higher collagen deposition on softer PCL scaffolds. Statistical analysis is carried out as mentioned in the experimental section where asterisks indicate alpha value $p < 0.01$ as "**" and $p < 0.0001$ as "****". $n = 3$.

disruption is not clear. It has also been shown that IFNγ promotes epithelial restitution by enhancing barrier function and wound healing.[38] Although, the combination of TNF-α+IFNγ did slightly increase in apparent permeability on the models. Nevertheless, the combination of TNF-α+IFNγ has been shown to destroy tight junctions of airway epithelial cells.[39] The difference in response of H441 cells to cytokines could be due to the tumor cell line nature. Thus, future experiments need to be conducted using primary alveolar epithelial cells to understand cytokine effects on barrier properties.

2.4. Overall Collagen Production

Indirect quantification of total collagen content was determined by hydroxyproline assay after 7 and 21 days of alveolar-capillary barrier on PCL meshes and control. The high content of hydroxyproline was detected on 2 µm PCL meshes after 7 and 21 days, which indicates a significantly higher amount of collagen deposition (**Figure 5**). To eliminate the possibility of endothelial mesenchymal transition as a cause of enhanced collagen content on the PCL meshes, immunohistochemistry analysis of alveolar-capillary barriers on days 7 and 21 was conducted for the mesenchymal marker, α-smooth muscle actin (α-SMA), and endothelial cell marker, CD31. It was observed that endothelial cells of day 7 alveolar-capillary barrier models on both PCL and PET membranes did not express the mesenchymal marker α-SMA and widely expressed CD31 (Figure 5A,B,G,F). However, on day 21 co-culture models, 94.80% ± 4.19% of endothelial cells expressed α-SMA on the control PET membrane compared to 28.25% ± 9.92% of

endothelial cells on the PCL mesh, while still both the models expressed CD31 endothelial marker (Figure 5C–E,I,H). The simultaneous expression of α-SMA and CD31 indicates that the endothelial cells are not completely transitioned into mesenchymal cells on both PCL and PET membranes, however, the effect of transition was more prominent in PET membranes. Therefore, it can be concluded that endothelial mesenchymal transition does not contribute to the increased collagen deposition on PCL meshes compared to the PET (Figure 5J). The optimum collagen deposition on PCL mesh can be attributed to enhanced cellular response and interaction with the nanofiber meshes that share a close structural resemblance to the native ECM.[40] The ability of cells to remodel and interact with electrospun nanofiber meshes has been investigated by Anjum et al., where enhanced collagen deposition on electrospun PCL meshes by dermal progenitor cells was observed.[41] Furthermore, the ability of cells to sense and uniquely respond to flat and fibrillar microenvironments was studied by Baker et al, and their findings suggest that cellular behavior such as proliferation and elongation are better on fibrous material compared to flat surfaces.[42] This further substantiates the influence of substrate structure and elastic modulus on cell behavior and signifies the importance of recapitulating the architecture of natural BM to achieve an in vitro model as close as possible to the lung parenchyma.

2.5. Neutrophil Migration

Neutrophils are the first line of defense during inflammation. These circulating immune cells undergo a cascade of steps

**ADVANCED
SCIENCE NEWS**
www.advancedsciencenews.com

**ADVANCED
BIOLOGY**
www.advanced-bio.com
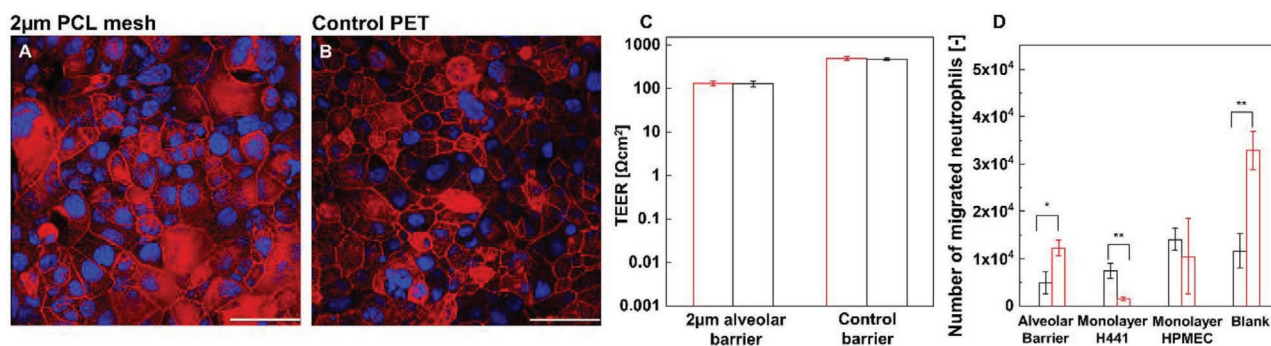
Figure 6. Effect of incubating alveolar–capillary barrier models for 2 h with IL-8 (10 ng mL^{-1}) on barrier integrity is investigated by immune-staining of epithelial tight junctions ZO-1 and TEER measurements where A,B) CLSM images of continuous and undisrupted immune-stained epithelial tight junctions ZO-1 (red) and cell nucleus (DAPI-blue) after IL-8 addition; C) difference in TEER values before (red) and after (black) addition of IL-8 on alveolar barrier models on both 2 μm PCL and PET membranes is not observed; D) neutrophil transmigration across different model systems in presence of chemokine IL-8 (10 ng mL^{-1}) is quantified by FACS, for control 3 μm pore PET membranes (black) and PCL nanofibrous mesh (red) with 1.45 μm pore size which included alveolar–capillary barrier, monoculture H441, HPMEC, and bare membranes as blank. In the presence of IL-8, high porosity contributes to abundant neutrophil migration across the blank PCL meshes. Irrespective of the membranes used, the extent of migration is higher across HPMEC monolayer in the presence of IL-8. The integrity of H441 on PCL meshes prevents abundant migration in contrast to the standard PET membranes. Compared to the control membranes, the increased transmigration across the alveolar-capillary barrier on PCL meshes makes it a closer representation of the native counterpart. Statistical analysis is carried out as mentioned in the experimental section where asterisks indicate alpha value $p < 0.5$ as "*" and $p < 0.01$ as "**", $n = 3$.

where they get captured on the endothelial cell surface and transmigrate towards the injured tissue by crossing across the endothelial layer and BM under the influence of chemo- and cytokines (TNF-α, IL-8, endotoxins LPS).[43] It is essential to know whether the intricate and interconnected pores present in the 2 μm PCL nanofibrous meshes with an equivalent pore diameter of 1.45 μm allow the migration of neutrophils compared to the conventionally used PET membranes with 3 μm pores. To exclude the possibility of barrier disruption by IL-8, co-culture models were tested for the immune-staining of tight junction ZO-1 and the TEER properties before and after incubation of 2 h with IL-8 (10 ng mL^{-1}). At this concentration of IL-8 and incubation period similar to neutrophil experiments, the tight junctions and TEER were intact (**Figure 6**A–C).

The neutrophil migration experiments were performed on the alveolar-capillary barrier established on 2 μm PCL meshes and controls with 3 μm etched pores under the absence and presence of chemokine IL-8. Co-cultures were compared with bare membranes, endothelial monolayers (seeded on the apical side of the membrane), and epithelial monolayers (seeded on the basal side of the membrane) and fluorescence-activated cell sorting (FACS) analysis was conducted to measure the extent of neutrophil migration (Figure S7, Supporting Information). From the FACS analysis, it could be inferred that few or no neutrophil migration was observed in the absence of IL-8 on both 2 μm PCL meshes and control (Figure S8, Supporting Information). The FESEM images corroborated the effect (Figure S9, Supporting Information). However, in the presence of IL-8, neutrophils migrated across all models. Under the influence of IL-8, the extent of migration was higher in the case of bare 2 μm PCL meshes in comparison to control (Figure 6D), while in monocultures an increased number of neutrophils migrated across endothelial monolayer for both the membranes. Increased percentage of neutrophil migration across endothelial monolayers can be explained due to the

presence of adhesion molecules namely selectins on the surface of endothelial cells which enhances neutrophil adhesion.[44] Surprisingly in the presence of IL-8, significantly higher transmigration of neutrophils across epithelial monolayers on control was observed (Figure 6D) in comparison to the PCL mesh. This could be possible only if epithelial barrier integrity on control membranes was challenged.[13] For the co-culture models, migration across the PCL meshes superseded the control membranes. A similar observation was made by SEM analysis of the meshes and controls (**Figure 7**).

This is the first study that shows successful neutrophil migration across the alveolar-capillary barrier models on electrospun ultra-thin PCL nanofibrous meshes. To the best of our knowledge, a minimum pore size of 3 μm is required for neutrophil migration.[18,21] Despite the smaller equivalent pore diameter of 1.45 μm of the 2 μm PCL meshes, neutrophil migration under the influence of IL-8 was observed. The migration of neutrophils across dense and narrow constrictions is a debatable field with unanswered questions regarding the exact mechanism used to traverse such regions. It is known that neutrophils pass through extremely narrow spaces by remodeling their nucleus.[45] Independent of the elastic modulus of the substrate as long as the multilobed nucleus of neutrophils (2 μm in diameter with 0.5 μm nucleus segments) can deform its size and shape, the neutrophil can squeeze through extremely narrow regions.[46] However, conventional etched PET membranes of pore size smaller than 3 μm inhibit neutrophil migration[21,46] and greater than 3 μm can lead to unwanted endothelial and epithelial transmigration.[12,13] Comparatively, ultra-thin PCL meshes allow successful establishment of the alveolar barrier where opposite cell layers are spatially separated and despite the smaller pore diameter, the relatively high permeability due to interwoven mesh allows for successful migration of neutrophils, demonstrating a paradigm shift in neutrophil transmigration studies.

**ADVANCED
SCIENCE NEWS**

www.advancedsciencenews.com

**ADVANCED
BIOLOGY**

www.advanced-bio.com
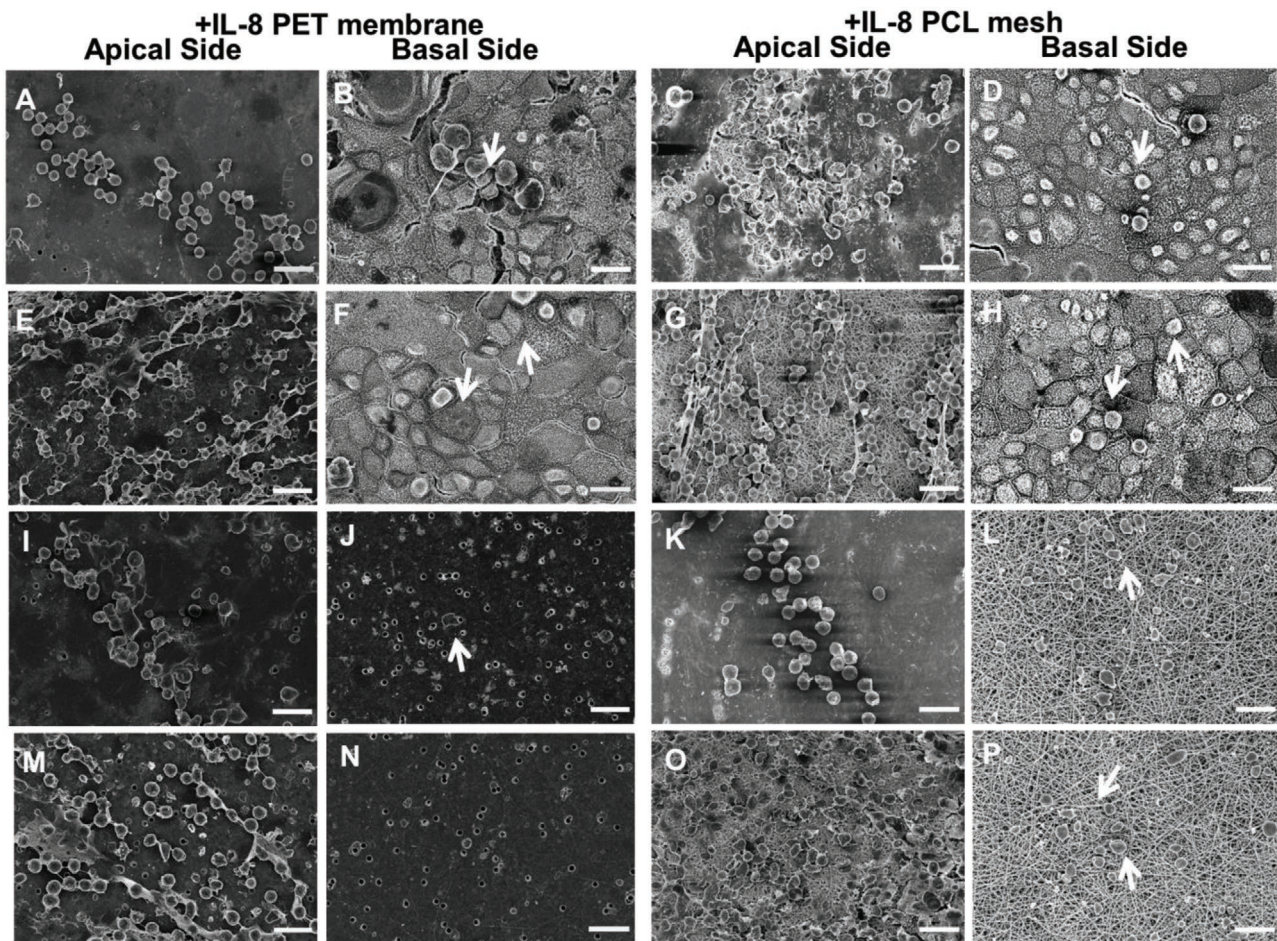
Figure 7. FESEM images depict transmigration of neutrophils on 10 μm PET membranes and 2 μm PCL nanofibrous meshes across A–D) alveolar-capillary barrier, E–H) monolayer H441 models, I–L) monolayer HPMEC models, and M–P) blank membranes, in the presence of IL-8. White arrows indicate transmigrated neutrophils, where the apical side indicates the neutrophil seeding side and the basal side as the transmigrated side. Scale bar: 50 μm.

3. Conclusion

In this study, the significance and influence of mimicking natural BM to establish stable in vitro alveolar–capillary barrier models have been validated by fabricating a stable in vitro model on ultra-thin 2 μm nanofibrous PCL meshes for 21 days. The highly porous PCL nanofibrous meshes were mechanically stable to support and maintain an integral alveolar–capillary barrier without cell infiltration and requirements of additional external support meshes. The importance of mimicking the natural BM both in structure and thickness has been highlighted by comparing 2 μm nanofibrous PCL and 10 μm dense PET membranes. The thickness and structure of the BM mimic play an important role where models on 2 μm PCL meshes exhibit improved barrier properties, collagen deposition, and inflammatory response such as transmigration of neutrophils. Successful neutrophil transmigration across the alveolar–capillary barrier on the ultra-thin electrospun PCL meshes with lower than 3 μm pore size compared to standard requirements of greater than 3 μm etched pores corresponds to the native response under inflammatory conditions. Fibrous nature, thickness, pore size, and porosity need to be considered

in the design of synthetic BM mimics as these features regulate major cellular behavior for the formation of an efficient and integral barrier model that significantly replicates the in vivo characteristics. The fabricated PCL nanofibrous meshes are characterized by the appropriate thickness and pore sizes that allow molecular diffusion, integral cellular tight junctions, immune cell transmigration as well as maintenance of distinct cell monolayers on opposite sides without the need for mechanical support. The developed alveolar-capillary barrier model closely represents the native form and thus provides a beneficial platform to study cellular behavior, as well as evaluate drug response and toxic particles.

As an outlook, PCL blended with different ECM components[47] will be used to tune the fiber diameter and material properties[27b,49] to represent the normal or disease state of the alveolar–capillary barrier.

4. Experimental Section

Cells and Cell culture: Primary Human Pulmonary Microvascular Endothelial Cells (HPMEC C-12281) and microvascular endothelial cell

culture media (C-22120) were purchased from Promocell. The Human lung adenocarcinoma cell line NCI-H441 (ATCC-HTB-174) was purchased from ATCC. RPMI-1640 (21875), penicillin/streptomycin (15140), trypsin (12604) were obtained from Thermo Fischer Scientific. Gelatin (G9391) was purchased from Sigma Aldrich and Fetal Bovine Serum-FBS (5181 BH) was obtained from Biowest.

HPMEC was maintained in 2 wt% gelatin-coated culture flasks with endothelial cell growth medium MV at 37 °C and 5% CO_2. When cells achieved 85% confluency they were subcultured or used for further experiments. HPMEC, not more than passage 4 was used. The cell line NCI-H441 was cultured in RPMI-1640 supplemented with 1%penicillin/streptomycin and 10% FBS at 37 °C and 5% CO_2. Subculture and further use in experiments were carried out when these cells were 80–85% confluent. NCI-H441 cells below passage 20 were used for experiments.

Electrospinning: PCL (poly(caprolactone) M_n 80 000, $M_w/M_n <$ 2) (440744 Sigma Aldrich) pellets were weighed and dissolved in HFIP (1,1,1,3,3,3-Hexafluoro-2-propanol) (105 228 Sigma Aldrich) to obtain 5 wt% solution. 10 µL of 1% TFA (Trifluoroacetic acid) (T6508 Sigma Aldrich) was added additionally to increase solution conductivity. The earthed spinneret was comprised of a syringe with a flat-tipped 27 gauge needle filled with the respective polymer solution. A 20 cm × 20 cm collector with aluminum foil was connected to a high voltage supply. When the induced electric field was high enough to overcome the surface tension of the droplet and promote elongation of the Taylor cone at the spinneret resulting in fiber formation deposited on the collector as meshes. The spinning parameters were optimized to 21 kV, 15 cm (distance between collector and spinneret), and 0.35 mL h^{-1} to obtain homogenous nanofibrous meshes. The time of electrospinning was 1 min for 2 µm thin meshes.

Mesh Characterisation Determination of Mesh Thickness: WYKO NT2000 profiling system was used to measure the thickness of ultra-thin samples. Vertical Scanning Interferometry mode enabled measurement of the step created by the mesh surface. Meshes were placed on a silicon wafer and white light was passed through the samples. A single scan with 1× speed, primary scan options of 15 µm back scan, 10 µm length, and modulation threshold of 2% was selected. The in-built software determines the size of the step created by the membrane on the silicon wafer by measuring the difference in height of the upper and lower surface of the meshes which indicates the thickness.

Determination of Fiber Diameter and Mesh Pore Size: Scanning Electron Microscopy (SEM), using S-4800 ultrahigh-resolution SEM (HITACHI, Japan) was performed to obtain images of the meshes. A 10 nm layer of Au/Pd was sputtered on the fibers and an accelerating voltage of 20 kV and a working distance of 10 to 15 mm were used to analyze the membranes. The images were later analyzed using the diameterJ plugin of ImageJ to determine the fiber diameter and pore size.

Determination of Tensile Stress: AllroundLine, Zwick Roell (Germany) tensile tester was used to study the deformation properties of the meshes under the applied force of 100 N cell load. A customized method was improvised to insert the ultra-thin PCL nanofibrous meshes into the tensile tester clamps by electrospinning on aluminum frames of 2 cm × 1 cm dimensions. The frame provided support to fix the meshes to the clamps while the edges of the frames were cut off and the deformation measured was solely due to the mesh. The Young's modulus was obtained by calculating the slope of stress over strain within 10% linear strain region.

3D Printed Transwell Inserts: Fabricated PCL meshes were supported on custom 3D printed inserts made in-house. A prototype of the insert was designed using Autodesk inventor professional 2017. The designs were printed by polyjet 3D printing (Stratasys, Objet Eden 260 V) using a mixture of two polymers. The first polymer was photosensitive & acrylate-based (Stratasys, RGD810) and the second (Stratasys, SUP705) was required to support the static mixers during the process of printing. After printing, 1 M NaOH was used to dissolve the supporting polymer.

Establishing Alveolar–Capillary Barrier: Corning insert (3470 Costar) were used as controls and electrospun nanofibrous meshes were placed onto custom 3D printed transwell inserts fabricated in-house using VeroClear material.[49]

Electrospun meshes were cut into 20 mm discs and immersed in PBS before carefully being peeled from the aluminum foils they were collected on, using forceps. The membranes were then immersed in ethanol for sterilization and placed in 1 × PBS and immobilized onto the transwell inserts (Figure S4, Supporting Information). Further treatment for adhesion was not required as the adhesion of the hydrophobic PCL meshes onto the hydrophobic insert was merely due to physical attraction. Once fixed smoothly, the membranes were allowed to air-dry, followed by three consecutive 5 min wash with PBS. The fixed membranes were UV sterilized for 30 min on opposite sides each. Following sterilization, inserts were plasma-treated using the PVA Tepla Plasma System 100 device at 20 watts, 40 mL min^{-1} for 30 s, followed by incubation in ECM mixture of Collagen I (5005 Advanced Biomatrix) (60%), fibronectin (30%) (F2006 Sigma Aldrich), and laminin (10%) (L6274 Sigma Aldrich), for 3 h at 37 °C.

To achieve alveolar–capillary barrier on the meshes, the inserts were inverted in a 12 well plate and a 60 µL cell suspension droplet of 7 × 10^4 HPMEC was seeded on the membranes and incubated for 2 h at 37 °C and 5% CO_2. The inserts were re-inverted in a 24 well followed by the addition of 1000 µL endothelial cell growth medium in the basal chamber and 250 µL in the apical chamber. The next day, 250 µL of 10^5 NCI-H441 cell suspension was seeded on the luminal side. 1 µM dexamethasone (D4902 Sigma Aldrich) was added to the apical chamber after 3 days of co-cultivation. Media change was done on alternate days and included 1000 µL endothelial growth medium in the basal chamber along with 250 µL RPMI with 1 µM dexamethasone. For monocultures, cell seeding and media change were done similarly.

Trans-Epithelial Electrical Resistance (TEER): Barrier properties of the alveolar-capillary barrier and monoculture models on nanofibrous PCL meshes and control were carried out regularly using the EVOM2 Epithelial Tissue Volt/Ohmmeter purchased from World Precision Instruments (Germany). Standard STX2 chopstick electrodes were used where one electrode arm was placed in the lower well and the other in the upper well. The measured resistance (Ω) across the cell layer was subtracted by the measured resistance of blank meshes. This value was multiplied by the cell growth area (0.33 cm²) to calculate the TEER (Ω cm²).

Permeability Assay: The barrier integrity of the alveolar-capillary in terms of paracellular transport was analyzed using 70 kDa FITC-dextran (46 945 Sigma Aldrich) and 66 kDa FITC-albumin (A9771 Sigma Aldrich). In addition to paracellular transport, FITC-albumin was used for the assessment of cellular transcytosis. For permeability assay, 150 µL of 500 µg mL^{-1} of the tracer molecule in MEM (51 200 038 Thermofischer Scientific) media was added to the apical chamber and 500 µL of MEM media was added to the basal chamber. At different time intervals of 15, 30, 45, 60, 90, 120, 180 min respectively, 50 µL of the sample was collected from the basal chamber and replaced by 50 µl of fresh MEM media. The fluorescence of the collected samples was measured in a plate reader (SpectraMax M3, Molecular devices) at excitation wavelength 492 nm and emission wavelength 518 nm. The cumulative amount of FITC-dextran and FITC-albumin measured in the basal chamber was plotted against time. The apparent permeability coefficient (cms^{-1}) was calculated using the formula 2, where A is the surface area of filter (0.33 cm²), C_0 is initial concentration of FITC-dextran and albumin added in the apical chamber and dQ/dt was the cumulative amount collected in the basal chamber after 60 min.

$$(1/(A * C_0)) * (dQ/dt) \qquad (2)$$

Mass flux of FITC-dextran on blank PCL and PET membrane was calculated by dividing total amount of molecules collected in the lower chamber after 60 min by the initial amount added in the apical chamber. This was expressed in terms of mean percentage ± percent standard error.

Immunocytochemistry: Cells on meshes were fixed with 4% paraformaldehyde (PFA A3813 PanReac Applichem) at room temperature (RT) for 15 min followed by permeabilization with 0.25%

**ADVANCED
SCIENCE NEWS**

www.advancedsciencenews.com

**ADVANCED
BIOLOGY**

www.advanced-bio.com

Triton-X (T9284 Sigma Aldrich) for 10 min. Subsequently, the samples were blocked for 60 min with a solution of 5% BSA (A2153 Sigma Aldrich) in PBS. To visualize the cell-cell junctions of HPMEC, samples were incubated with primary antibody CD31 (1:50 ab9498 Abcam) for 1 h followed by PBS wash. Secondary antibody goat anti-mouse Alexa Flour 594-conjugated IgG (1:200 A11005 Thermo Fischer Scientific) was added for 1 h followed by washing with PBS. To stain the H441 cells junctional complexes E-cadherin, the samples were incubated with an E-cadherin antibody (1:200 24E10 Cell Signaling Technology) at 4 °C overnight. The next day, samples were washed with PBS followed by the addition of the secondary goat anti-rabbit Alexa Flour 488 conjugated IgG (1:400 A11034 Thermo Fischer Scientific) for 1 h. To visualize tight junctions and mesenchymal smooth muscle actin, models were incubated with primary ZO-1 antibody (1:100 61-7300 Thermofischer Scientific) or α-SMA (1:50 A5228 Sigma Aldrich) at 4 °C overnight. The next day, the addition of secondary goat anti-rabbit Alexa Flour 594 conjugated IgG (1:200 ab150080 Abcam) or secondary goat anti-mouse Alexa Flour 488 conjugated IgG (1:200 ab150113 Abcam) for 2 h. This was followed by PBS wash and addition of DAPI (1:1000 D1306 Molecular probes) to counterstain the nuclei with subsequent PBS washing steps. All the aforementioned PBS washing steps included 3× wash for 5 min each. The stained samples were carefully cut off from the inserts using a surgical scalpel (1868278 Braun) and placed between two glass coverslips (631-0153 VWR) and observed with CLSM (CLSM Leica TCS SPE, Leica, Germany).

Treatment with TNF-α and IFNγ: Ten days cultivated alveolar-capillary barrier models on PCL meshes and control were exposed to cytokine TNF-α (10 ng mL^{-1} ab9642 Abcam) and IFNγ (30 ng mL^{-1} 300-02 Peprotech) by introducing it in the apical chamber for 24 h. These concentrations were chosen based on similarities to clinical values in bronchial alveolar lavage and corresponding literature reports,[50] where this concentration range influences the epithelial tight junctions. Treatment was followed by a collection of media supernatant from treated and untreated models. The media supernatant was collected on ice and centrifuged at 4 °C, 400 rpm for 3 min to remove cell debris. The supernatant was collected and stored at −80 °C until further analysis. Additionally, the permeability assay was conducted on the treated and untreated models using 70 kDa FITC-dextran.

Enzyme-Linked Immunosorbent Assay (ELISA): Culture supernatants of TNF-α, IFNγ, and their combination-treated models and untreated alveolar-capillary barrier models on PCL nanofibrous meshes and control were collected to analyze the presence of intercellular adhesion molecule 1 (sICAM). The concentration sICAM was measured by human sICAM Elisa kit (BMS201 Invitrogen) and instructions provided by the manufacturer were followed. In brief, collected media samples from the models were diluted 1:5 and along with standards were added to the antibody-coated 96 well plates followed by the addition of HRP conjugated anti-antibody to human sICAM and incubated for 2 h. This was followed by a washing step to remove unbound HRP conjugates. A TMB substrate solution that reacts with HRP was added and incubated for 10 min for color development, followed by the addition of stop solution. The protein concentrations were determined by streptavidin-HRP colorimetric reaction where the optical density at 450 nm was measured using a microplate reader (SpectraMax M3, Molecular devices).

Determination of α-SMA Positive Cells: To quantify positive cells expressing α-SMA, 850 endothelial cells were quantified on each PCL and PET membrane alveolar model on day 21. The CLSM images were analyzed using the cell counter plug-in of ImageJ software. Cells expressing α-SMA along with the total number of cells were counted manually using the cell counter tool. The α-SMA positive cells were expressed as a percentage of positive cells ± standard percent error.

Hydroxyproline Assay: To quantify total collagen content produced by cells on the alveolar-capillary barrier models on PCL meshes and control, a hydroxyproline assay kit (MAK008 Sigma Aldrich) was used. Sample preparation and protocols were followed according to the manufacturers' instructions. Briefly, the models were homogenized at 120 °C for 3 h in a 1:1 mixture of hydrochloric acid and water, followed

by supernatant collection in a 96 well plate. The supernatant was left to dry at 60 °C. The dried samples were treated with 4-(dimethylamino) benzaldehyde reagent, which gives a colorimetric product proportional to the concentration of hydroxyproline. The optical density was measured at 560 nm using a microplate reader (SpectraMax M3, Molecular devices).

Isolation of Neutrophils and Migration: Neutrophils were freshly isolated from human blood drawn from a healthy donor's vein. The presented experimental procedure was approved by the Ethics Committee of Aachen University Hospital (Permission No: EK150/09, Oct. 6, 2009). All adult participants gave written informed consent before having taken their venous blood samples. In brief, a syringe filled with 5 mL of 3.13% sodium citrate, to prevent blood coagulation, was used to draw 20 mL of blood from the vein. The blood was further diluted 1:1 with PBS followed by slow addition of 20 mL diluted blood along the sides of the tube into 20 mL of Pancoll human (PanBiotec P0460500) solution. To form separate layers of the blood, the solution was further centrifuged at 300 rpm, 30 min without break. All the layers except the red pellet were aspirated and the pellet was treated with erythrocyte lysis buffer followed by centrifugation at 300 rpm for 5 min and re-suspension in erythrocyte buffer. After the erythrocytes were removed, the pellet was re-suspended in RPMI with only 0.2%BSA. In the apical chamber, 2×10^6 neutrophil cells in 150 µL volume RPMI were seeded. The lower chamber was filled with 500 µL RPMI. Where required, 10 ng mL^{-1} IL-8 (200-08 Peprotech) chemokine was added to the lower chamber of the models. All the models were incubated for 2 h at 37 °C, followed by the collection of media from the lower wells to analyze the number of migrated cells using FACS. Migration experiments were carried out on 2 µm PCL meshes and 10 µm thick control with 3 µm pore size (Greiner-bio one 662630).

Fluorescence-Activated Cell Sorting (FACS): The quantification of migrated neutrophils was carried out using the FACS canto analyzer (Becton Dickinson). The cells in the collected media from the migration experiments were fixed using 4% PFA and re-suspended in 400 µL PBS to analyze using FACS. A gating strategy was set up to detect neutrophils using Forward Scatter and Side Scatter which enabled counting of neutrophils based on cell size and granularity. Collected data from the counting experiments were analyzed using the FCS Express software and graphs were plotted to verify the number of neutrophils that migrated across each model system including bare membranes, monolayer HPMEC, monolayer H441, and the alveolar-capillary barrier.

Electron Microscopy: FESEM was performed using S-4800 ultra-high resolution SEM (HITACHI, Japan) to analyze characteristics of electrospun fibers as well as cell morphology and neutrophil migration on the nanofibrous PCL meshes and control. The samples were sputtered with a 6 nm layer of Au/Pd using Leica EM ACE600. An accelerating voltage of 2 kV and a working distance of 10–15 mm were used. For samples with cells, a series of drying steps using ethanol (19J214027 VWR) (30%, 50%, 70%, and 100%) for 10 min each were carried out followed by drying using Hexamethyldisilazane (H4875 Sigma Aldrich) for another 10 min. After drying, the samples were sputtered with Au/Pd and used for analysis.

TEM was performed to investigate the cross-sections of the alveolar-capillary barrier models. Samples were fixed with 2.5% glutaraldehyde overnight at 4 °C, followed by washing with PBS, and incubated for 2 h with 1% OsO4 (Science services). After this treatment, the samples were dehydrated in ethanol and embedded in a resin. Ultra-thin 70 nm sections were cut using an ultramicrotome (Leica, Germany). The samples were observed by HT7800 (HITACHI, Japan) at an accelerating voltage of 20–120 kV and pixel resolution of 0.36 nm.

Statistical Analysis: All data analyzed were expressed as mean±standard deviation, unless stated otherwise. Three individual experiments were carried out for statistical analysis and as stated in figure caption. The groups were analyzed for statistical differences using hypothesis tests in Origin software by using the two-sample *T*-test for means. An alpha value *p* less than 0.05 was considered statistically significant. The *p* values are indicated in the figure captions where necessary.

Supporting Information

Acknowledgements

Conflict of Interest

The authors declare no conflict of interest.

Data Availability Statement

The data that support the findings of this study are available from the corresponding author upon reasonable request.

Keywords

[1] a) M. Letko, A. Marzi, V. Munster, *Nat. Microbiol.* **2020**, *5*, 562; b) D. Gurwitz, *Drug Dev. Res.* **2020**, *81*, 1073; c) H. Zhang, J. M. Penninger, Y. Li, N. Zhong, A. S. Slutsky, *Intensive Care Med.* **2020**, *46*, 586.

[2] a) V. E. Calderon, G. Valbuena, Y. Goez, B. M. Judy, M. B. Huante, P. Sutjita, R. K. Johnston, D. M. Estes, R. L. Hunter, J. K. Actor, J. D. Cirillo, J. J. Endsley, *PLoS One* **2013**, *8*, e63331; b) R. Ito, T. Takahashi, I. Katano, M. Ito, *Cell Mol. Immunol.* **2012**, *9*, 208; c) S. Pérez-Rial, Á. Girón-Martínez, G. Peces-Barba, *Archivos de Bronconeumología* **2015**, *51*, 121.

[3] a) K. L. Fonseca, P. N. S. Rodrigues, I. A. S. Olsson, M. Saraiva, *PLoS Pathog.* **2017**, *13*, e1006421; b) A. J. Miller, J. R. Spence, *Physiology* **2017**, *32*, 246.

[4] a) M. I. Hermanns, R. E. Unger, K. Kehe, K. Peters, C. J. Kirkpatrick, *Lab. Invest.* **2004**, *84*, 736; b) D. Huh, B. D. Matthews, A. Mammoto, M. Montoya-Zavala, H. Y. Hsin, D. E. Ingber, *Science* **2010**, *328*, 1662; c) S. G. Klein, J. Hennen, T. Serchi, B. Blömeke, A. C. Gutleb, *Toxicol. In Vitro* **2011**, *25*, 1516; d) A. Jain, R. Barrile, A. D. van der Meer, A. Mammoto, T. Mammoto, K. De Ceunynck, O. Aisiku, M. A. Otieno, C. S. Louden, G. A. Hamilton, R. Flaumenhaft, D. E. Ingber, *Clin. Pharmacol. Ther.* **2018**, *103*, 332.

[5] T. J. Franks, T. V. Colby, W. D. Travis, R. M. Tuder, H. Y. Reynolds, A. R. Brody, W. V. Cardoso, R. G. Crystal, C. J. Drake, J. Engelhardt, M. Frid, E. Herzog, R. Mason, S. H. Phan, S. H. Randell, M. C. Rose, T. Stevens, J. Serge, M. E. Sunday, J. A. Voynow, B. M. Weinstein, J. Whitsett, M. C. Williams, *Proc. Am. Thorac. Soc.* **2008**, *5*, 763.

[6] a) T. Hussell, T. J. Bell, *Nat. Rev. Immunol.* **2014**, *14*, 81; b) J.-H. Lee, D. H. Bhang, A. Beede, T. L. Huang, B. R. Stripp, K. D. Bloch, A. J. Wagers, Y.-H. Tseng, S. Ryeom, C. F. Kim, *Cell* **2014**, *156*, 440; c) J. R. Teijaro, K. B. Walsh, S. Cahalan, D. M. Fremgen, E. Roberts, F. Scott, E. Martinborough, R. Peach, M. B. A. Oldstone, H. Rosen, *Cell* **2011**, *146*, 980.

[7] R. Kalluri, *Nat. Rev. Cancer* **2003**, *3*, 422.

[8] a) S. Inoue, R. P. Michel, J. C. Hogg, *J. Ultrastruct. Res.* **1976**, *56*, 215; b) A. B. Gorin, P. A. Stewart, *J. Appl. Physiol.* **1979**, *47*, 1315; c) E. R. Weibel, *Am J. Respir. Crit. Care Med.* **2015**, *191*, 504.

[9] a) G. R. Ainslie, M. Davis, L. Ewart, L. A. Lieberman, D. J. Rowlands, A. J. Thorley, G. Yoder, A. M. Ryan, *Lab Chip* **2019**, *19*, 3152; b) P. G. Miller, C. Y. Chen, Y. I. Wang, E. Gao, M. L. Shuler, *Biotechnol. Bioeng.* **2020**, *117*, 486; c) J. Shrestha, M. Ghadiri, M. Shanmugavel, S. R. Bazaz, S. Vasilescu, L. Ding, M. E. Warkiani, *Organs-on-a-Chip* **2020**, *1*, 100001; d) J. D. Stucki, N. Hobi, A. Galimov, A. O. Stucki, N. Schneider-Daum, C. M. Lehr, H. Huwer, M. Frick, M. Funke-Chambour, T. Geiser, O. T. Guenat, *Sci. Rep.* **2018**, *8*, 14359.

[10] a) J. Geys, L. Coenegrachts, J. Vercammen, Y. Engelborghs, A. Nemmar, B. Nemery, P. H. Hoet, *Toxicol. Lett.* **2006**, *160*, 218; b) S. Dekali, C. Gamez, T. Kortulewski, K. Blazy, P. Rat, G. Lacroix, *Toxicol. Rep.* **2014**, *1*, 157; c) D. Lee, M. Chambers, *F1000Research* **2019**, *8*, 357; d) A. Nishiguchi, S. Singh, M. Wessling, C. J. Kirkpatrick, M. Moller, *Biomacromolecules* **2017**, *18*, 719.

[11] a) S. Musah, A. Mammoto, T. C. Ferrante, S. S. Jeanty, M. Hirano-Kobayashi, T. Mammoto, K. Roberts, S. Chung, R. Novak, M. Ingram, *Nat. Biomed. Eng.* **2017**, *1*, 0069; b) N. Pouliot, H. B. Pearson, A. Burrows, In *Madame Curie Bioscience Database*, Landes Bioscience, Austin, TX **2013**.

[12] E. Vandenhaute, A. Drolez, E. Sevin, F. Gosselet, C. Mysiorek, M.-P. Dehouck, *Lab. Invest.* **2016**, *96*, 588.

[13] A. Weppler, D. Rowter, I. Hermanns, C. J. Kirkpatrick, A. C. Issekutz, *Exp. Lung Res.* **2006**, *32*, 455.

[14] a) N. A. Maniatis, M. Kardara, D. Hecimovich, E. Letsiou, M. Castellon, C. Roussos, V. Shinin, E. G. Votta-Vellis, D. E. Schwartz, R. D. Minshall, *Pulm. Circ.* **2012**, *2*, 452; b) Y. Jin, S.-J. Lee, R. D. Minshall, A. M. K. Choi, *Am. J. Physiol.: Lung Cell. Mol. Physiol.* **2011**, *300*, L151; c) P. M. Potey, A. G. Rossi, C. D. Lucas, D. A. Dorward, *The Journal of pathology* **2019**, *247*, 672; d) J. Milara, G. Juan, T. Peiró, A. Serrano, J. Cortijo, *Respiration* **2012**, *83*, 147.

[15] K. P. Steinberg, J. A. Milberg, T. R. Martin, R. J. Maunder, B. A. Cockrill, L. D. Hudson, *Am J. Respir. Crit. Care Med.* **1994**, *150*, 113.

[16] R. L. Zemans, S. P. Colgan, G. P. Downey, *Am. J. Respir. Cell Mol. Biol.* **2009**, *40*, 519.

[17] E. Kolaczkowska, P. Kubes, *Nat. Rev. Immunol.* **2013**, *13*, 159.

[18] K. Wolf, M. Te Lindert, M. Krause, S. Alexander, J. Te Riet, A. L. Willis, R. M. Hoffman, C. G. Figdor, S. J. Weiss, P. Friedl, *J. Cell Biol.* **2013**, *201*, 1069.

[19] a) Y. Deng, J. A. Herbert, C. M. Smith, R. L. Smyth, *Sci. Rep.* **2018**, *8*, 6777; b) S. Kawa, S. Kimura, S.-i. Hakomori, Y. Igarashi, *FEBS Lett.* **1997**, *420*, 196.

[20] M. A. Morrissey, D. R. Sherwood, *J. Cell Sci.* **2015**, *128*, 1661.

[21] R . G. Rowe, S. J. Weiss, *Trends Cell Biol.* **2008**, *18*, 560.

[22] a) S. M. Park, H. Kim, K. H. Song, S. Eom, H. Park, J. Doh, D. S. Kim, *Biomaterials* **2018**, *169*, 22; b) X. Yang, K. Li, X. Zhang, C. Liu, B. Guo, W. Wen, X. Gao, *Lab Chip* **2018**, *18*, 486.

[23] M. Bartoš, T. Suchý, R. Foltán, *Biomed. Eng. Online* **2018**, *17*, 110.

[24] L. W. Welling, M. T. Zupka, D. J. Welling, *Physiology* **1995**, *10*, 30.

[25] T. Pasman, D. Grijpma, D. Stamatialis, A. Poot, *J. R. Soc., Interface* **2018**, *15*, 20180351.

[26] S. Murikipudi, H. Methe, E. R. Edelman, *Biomaterials* **2013**, *34*, 677.

[27] a) D. E. Discher, P. Janmey, Y.-l. Wang, *Science* **2005**, *310*, 1139; b) N. Higuita-Castro, M. T. Nelson, V. Shukla, P. A. Agudelo-Garcia, W. Zhang, S. M. Duarte-Sanmiguel, J. A. Englert, J. J. Lannutti, D. J. Hansford, S. N. Ghadiali, *Sci. Rep.* **2017**, *7*, 11623.

[28] J. J. Salomon, V. E. Muchitsch, J. C. Gausterer, E. Schwagerus, H. Huwer, N. Daum, C.-M. Lehr, C. Ehrhardt, *Mol. Pharmaceutics* **2014**, *11*, 995.

[29] E. E. Schneeberger, D. V. Walters, R. E. Olver, *J. Cell Sci.* **1978**, *32*, 307.

[30] M. I. Hermanns, R. E. Unger, K. Kehe, K. Peters, C. J. Kirkpatrick, *Lab. Invest.* **2004**, *84*, 736.

[31] R. Yumoto, S. Suzuka, K. Oda, J. Nagai, M. Takano, *Drug Metab. Pharmacokinet.* **2012**, *27*, 336.

[32] a) A. Churg, J. Dai, H. Tai, C. Xie, J. L. Wright, *Am J. Respir. Crit. Care Med.* **2002**, *166*, 849; b) V. M. Keatings, P. D. Collins, D. M. Scott, P. J. Barnes, *Am J. Respir. Crit. Care Med.* **1996**, *153*, 530; c) L. K. Lundblad, J. Thompson-Figueroa, T. Leclair, M. J. Sullivan, M. E. Poynter, C. G. Irvin, J. H. Bates, *Am J. Respir. Crit. Care Med.* **2005**, *171*, 1363.

[33] a) Q. Wang, G. R. Pfeiffer, T. Stevens, C. M. Doerschuk, *Am J. Respir. Crit. Care Med.* **2002**, *166*, 872; b) E. A. Kotteas, P. Boulas, I. Gkiozos, G. Tsoukalas, K. N. Syrigos, *Anticancer Res.* **2014**, *34*, 4665; c) H. Kim, J.-S. Hwang, C.-H. Woo, E.-Y. Kim, T.-H. Kim, K.-J. Cho, J.-M. Seo, S.-S. Lee, J.-H. Kim, *Exp. Mol. Med.* **2008**, *40*, 167.

[34] J. Kasper, M. I. Hermanns, C. Bantz, M. Maskos, R. Stauber, C. Pohl, R. E. Unger, J. C. Kirkpatrick, *Part. Fibre Toxicol.* **2011**, *8*, 6.

[35] a) H. Shirasaki, H. Watanabe, E. Kanaizumi, J. Sato, N. Konno, S. Narita, T. Himi, *Clin. Exp. Allergy* **2004**, *34*, 945; b) A. Nehmé, J. Edelman, *Invest. Ophthalmol. Visual Sci.* **2008**, *49*, 2030.

[36] M. P. Mendez, S. B. Morris, S. Wilcoxen, M. Du, Y. K. Monroy, H. Remmer, H. Murphy, P. J. Christensen, R. PaineIII, *Am. J. Physiol.: Lung Cell. Mol. Physiol.* **2008**, *294*, L807.

[37] S. Uhlig, Y. Yang, J. Waade, C. Wittenberg, A. Babendreyer, W. M. Kuebler, *Cell. Physiol. Biochem.* **2014**, *34*, 1.

[38] M. Ahdieh, T. Vandenbos, A. Youakim, *Am. J. Physiol.: Cell Physiol.* **2001**, *281*, C2029.

[39] C. B. Coyne, M. K. Vanhook, T. M. Gambling, J. L. Carson, R. C. Boucher, L. G. Johnson, *Mol. Biol. Cell* **2002**, *13*, 3218.

[40] a) S. Ferraris, S. Spriano, A. C. Scalia, A. Cochis, L. Rimondini, I. Cruz-Maya, V. Guarino, A. Varesano, C. Vineis, *Polymers* **2020**, *12*, 2896; b) J. Venugopal, S. Low, A. T. Choon, S. Ramakrishna, *J. Biomed. Mater. Res., Part B* **2008**, *84*, 34.

[41] F. Anjum, N. A. Agabalyan, H. D. Sparks, N. L. Rosin, M. S. Kallos, J. Biernaskie, *Sci. Rep.* **2017**, *7*, 10291.

[42] B. M. Baker, B. Trappmann, W. Y. Wang, M. S. Sakar, I. L. Kim, V. B. Shenoy, J. A. Burdick, C. S. Chen, *Nat. Mater.* **2015**, *14*, 1262.

[43] S. de Oliveira, E. E. Rosowski, A. Huttenlocher, *Nat. Rev. Immunol.* **2016**, *16*, 378.

[44] K. D. Patel, S. L. Cuvelier, S. Wiehler, *Semin. Immunol.* **2002**, *14*, 73.

[45] M. Salvermoser, D. Begandt, R. Alon, B. Walzog, *Front. Immunol.* **2018**, *9*, 2680.

[46] K. Wolf, M. Te Lindert, M. Krause, S. Alexander, J. Te Riet, A. L. Willis, R. M. Hoffman, C. G. Figdor, S. J. Weiss, P. Friedl, *J. Cell Biol.* **2013**, *201*, 1069.

[47] J. X. Law, L. L. Liau, A. Saim, Y. Yang, R. Idrus, *Tissue Eng. Regener. Med.* **2017**, *14*, 699.

[48] P. Zamprogno, S. Wüthrich, S. Achenbach, J. D. Stucki, N. Hobi, N. Schneider-Daum, C.-M. Lehr, H. Huwer, T. Geiser, R. A. Schmid, O. T. Guenat, *Commun. Biol.* **2021**, *4*, 168.

[49] L. Wang, Y. Ju, H. Xie, G. Ma, L. Mao, K. He, *Sci. Rep.* **2017**, *7*, 10918.

[50] a) M. Ahdieh, T. Vandenbos, A. Youakim, *Am. J. Physiol.: Cell Physiol.* **2001**, *281*, C2029; b) A. Youakim, M. Ahdieh, *Am. J. Physiol.: Gastrointest. Liver Physiol.* **1999**, *276*, G1279; c) J. E. Losa García, F. M. Rodríguez, M. R. Martín de Cabo, M. J. García Salgado, J. P. Losada, L. G. Villarón, A. J. López, J. L. Arellano, *Mediators Inflammation* **1999**, *8*, 43.